

Simulation of Blast-Induced Early-Time Intracranial Wave Physics leading to Traumatic Brain Injury

Paul A. Taylor

Department of Penetration Systems,
Sandia National Laboratories,
Albuquerque, NM 87185

Corey C. Ford

Department of Neurology,
University of New Mexico Health Sciences
Center,
Albuquerque, NM 87131-0001

The objective of this modeling and simulation study was to establish the role of stress wave interactions in the genesis of traumatic brain injury (TBI) from exposure to explosive blast. A high resolution (1 mm³ voxels) five material model of the human head was created by segmentation of color cryosections from the Visible Human Female data set. Tissue material properties were assigned from literature values. The model was inserted into the shock physics wave code, CTH, and subjected to a simulated blast wave of 1.3 MPa (13 bars) peak pressure from anterior, posterior, and lateral directions. Three-dimensional plots of maximum pressure, volumetric tension, and deviatoric (shear) stress demonstrated significant differences related to the incident blast geometry. In particular, the calculations revealed focal brain regions of elevated pressure and deviatoric stress within the first 2 ms of blast exposure. Calculated maximum levels of 15 KPa deviatoric, 3.3 MPa pressure, and 0.8 MPa volumetric tension were observed before the onset of significant head accelerations. Over a 2 ms time course, the head model moved only 1 mm in response to the blast loading. Doubling the blast strength changed the resulting intracranial stress magnitudes but not their distribution. We conclude that stress localization, due to early-time wave interactions, may contribute to the development of multifocal axonal injury underlying TBI. We propose that a contribution to traumatic brain injury from blast exposure, and most likely blunt impact, can occur on a time scale shorter than previous model predictions and before the onset of linear or rotational accelerations traditionally associated with the development of TBI.

[DOI: 10.1115/1.3118765]

1 Introduction

The yearly incidence of traumatic brain injuries (TBIs) in the United States has been estimated at 1.4 million people, including 50,000 deaths and 235,000 hospitalizations [1]. Military personnel and civilians can also incur TBI as a consequence of explosive blasts, and in recent wars the incidence of such injuries has increased dramatically. This increase can be attributed to the tactics of asymmetric warfare, where enemy combatants detonate improvised explosive devices targeting vehicles and exposed individuals, improvements in personnel armor, as well as trauma evacuation and emergency care, allowing survival of previously fatal injuries. Recent statistics from the conflict in Iraq show that several thousand United States soldiers have sustained TBI, 69% as a result of blasts [2,3]. Injuries sustained from blast exposure have been categorized into three major components: primary, secondary, and tertiary [4]. Primary blast injury is associated with direct exposure of the head and body to the blast wave. In secondary blast injury, debris is accelerated into the individual, while in tertiary injury the victim is thrown into stationary objects by the blast. Both of the latter mechanisms are comparable to the mechanical trauma that has been the subject of decades of clinical, experimental, and computational research. However, the role of primary blast exposure in the development of TBI remains less understood [5]. Primary blast may induce linear and rotational cranial accelerations, but the sharp wave front of blast overpres-

sure will also trigger complex wave motions, transmitted by the skull into the high water content viscoelastic brain.

Multiple, often coexisting pathologies, can underlie the consequences of TBI, including easily visualized damage from contusions and intraparenchymal or extra-axial hemorrhages. However, at least one-third of the deaths and poor outcomes of TBI are the result of traumatic axonal injury occurring at the microscopic level [6]. Most often referred to as diffuse axonal injury or DAI, this pathological finding actually defines a multifocal process that can be widespread throughout the white matter tracks and other areas of the brain [7]. DAI has been linked to dynamic deformations caused by linear and rotational accelerations [8–11]. In pig models rapid nonimpact inertial loading produced multifocal axonal injury throughout the brain [10]. Studies of the brain after TBI have shown cytoskeletal disruptions, changes in membrane permeability, and the development of axonal swelling that can be followed by axonal transections with terminal axon bulbs [6,9,12]. The idea that the severed axons seen after TBI were the result of mechanical tearing has been replaced by the realization that most transected axons have undergone a progressive self-destructive sequence after the initial traumatic insult [6,12–14]. DAI has been demonstrated by histopathology in TBI of all severities, and studies have inferred its presence by nonconventional magnetic resonance imaging (MRI) in brain injured patients with no other imaging signs of damage on routine brain Computed Tomography (CT) and MRI scans [15,16].

Can TBI occur without macroscopic damage and unassociated with large translational or rotational motions? Could complex wave interactions in the brain, after impact or blast, result in focal injury to axons and trigger the cascade of secondary events leading to transections and permanent neurological disabilities? Loss of consciousness and brain injury from assault with a blunt object

Contributed by the Bioengineering Division of ASME for publication in the JOURNAL OF BIOMECHANICAL ENGINEERING. Manuscript received February 11, 2008; final manuscript received February 26, 2009; published online April 27, 2009. Review conducted by Philip V. Bayly.

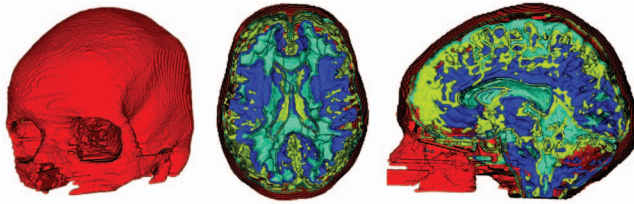


Fig. 1 Head model. Color code: red=bone, light blue=white matter, dark blue=gray matter, and yellow=cerebral spinal fluid. Voxel resolution: 1 mm³.

may not involve significant head motion. The different mechanisms of TBI and the variable outcomes for patients with similar levels of apparent injury led us to examine the role of wave action in delivering mechanical energy to critical brain regions.

The hypothesis underlying this study was that stress waves from blast exposure will transit and reflect within the intracranial contents of the head, resulting in focal areas of elevated stress great enough to cause axonal injury. The primary focus of this paper is to explore the role of intracranial wave mechanics in the genesis of traumatic brain injury from blast.

2 Modeling and Simulation Methodology

2.1 Computer Simulation Code. The blast simulations were carried out using the shock physics wave code CTH [17]. CTH is a Eulerian finite-volume computer code that is capable of tracking up to 20 materials simultaneously, simulating their interactions and material response as they undergo impact, blast loading, and penetration. The Eulerian description of material behavior is captured by means of a two-step solution scheme conducted for each time step. The first step consists of explicitly solving the finite-volume analogs of the Lagrangian equations of momentum and energy conservation, followed by a second step of rezoning of the computational mesh to construct Eulerian differencing. The Eulerian nature of the solution scheme in CTH permits the code to track large strain deformation and flow. A wide variety of nonlinear equation-of-state (EOS) and constitutive models describing strength and fracture behavior are available for use within CTH to describe complex material response during impact and blast wave loading. For the current study, we employed a variety of these models to represent the volumetric and deviatoric response of the materials in our head model and the surrounding air. These models are described in detail in Secs. 2.2 and 2.3.

2.2 Head Model. We constructed a head model based on the segmentation of high resolution photographic data, available from the Visible Human Project of the National Library of Medicine [18], with the assistance of colleagues at the Buffalo Neurological Center in Buffalo, NY. The photographic data consists of 0.33 mm thick axial slices of a cryogenically frozen human female. The axial slice image data were segmented using a pattern recognition algorithm applied to every third slice comprising the head above the mandible, resulting in a head model possessing a 1 mm cubic resolution for a total of 6,850,560 voxels (192 × 223 × 160). The slice segmentation data were assembled into a series of four voxel

bitmap files, representing the skull, white matter, gray matter, and cerebral spinal fluid, respectively, and read by the simulation wave code to generate material geometry of the head model. All major anatomic regions of the brain, including the cerebellum, corpus callosum, deep gray matter nuclei, brain stem, and ventricles, are included at 1 mm resolution, similar to that used in diagnostic MR imaging. Material properties of the head model include those for skull bone, gray and white matter, cerebral spinal fluid (CSF), and air in the sinuses. Figure 1 displays representative images of the head model as it is defined within the CTH wave code.

2.3 Material Models. Our simulation method incorporates EOS and constitutive models representing the four constituents of the head plus the surrounding air. The skull is represented by a compressible linear elastic perfectly plastic constitutive model and an accumulated strain-to-failure model to capture fracture, fit to data reported by Carter [19] for cortical bone. The models describing the volumetric and shear response of the skull are commonly understood and should require no further explanation. However, the failure model warrants further description where, in particular, a strain-to-failure fracture model was employed. This model introduces a damage variable D that is defined according to the relation

$$D(\mathbf{x}, t) = \int_0^t \frac{d\varepsilon^p}{\varepsilon_f^p} \quad (1)$$

where ε^p is the equivalent plastic strain, continuously updated at each time step, and ε_f^p denotes the critical value of equivalent plastic strain at fracture. $D=0$ denotes undamaged material, whereas failure is considered to have occurred whenever D reaches the value of 1. The damage variable is calculated for each material point in the skull at every time step, degrading both the plastic yield strength Y and fracture stress σ_f of the material in the following manner:

$$Y(\mathbf{x}, t) = Y_o[1 - D(\mathbf{x}, t)] \quad \text{and} \quad \sigma_f(\mathbf{x}, t) = \sigma_f^o[1 - D(\mathbf{x}, t)] \quad (2)$$

where Y_o and σ_f^o denote values of yield and fracture stress, respectively, for undamaged material. For the skull material properties, we have selected data reported by Carter [19] in which $Y_o = 95$ MPa, $\sigma_f^o = 77.5$ MPa, and $\varepsilon_f^p = 0.008$. The equivalent plastic failure strain was determined from Carter's data which showed a total failure strain of 0.016 (elastic plus plastic components) and a yield strain of 0.008. The plastic strain at failure is determined to be the difference between the two. The complete list of material property values for the skull appears in Table 1.

The white and gray matter are considered to be compressible viscoelastic materials and have been assigned constitutive models identical to those employed by Zhang et al. [20]. In particular, these tissues are represented by an elastic compressible equation-of-state model for the volumetric response and a generalized three-term Maxwell viscoelastic model for the deviatoric (shear) response. Specifically, the time-dependent shear modulus of the brain tissue is represented by the equation

Table 1 Elastic material properties

	Density (g/cc)	Bulk modulus (GPa)	Poisson's ratio	Yield stress (MPa)	Strain to failure (%)	Fracture stress (MPa)
Skull	1.412	4.82	0.22	95	0.8	77.5
White matter	1.04	2.37	0.49	-	-	-
Gray matter	1.04	2.37	0.49	-	-	-
CSF	1.00	1.96	0.50	-	-	-
Dry air	1.218×10^{-3}	1.00998×10^{-4}	0.5	-	-	-

Table 2 Viscoelastic material properties

	Short-term shear modulus G_o (KPa)	Long-term shear modulus G_∞ (KPa)	Decay constant β (s^{-1})
White matter	41.0	7.8	700
Gray matter	34.0	6.4	700

$$G(t) = G_\infty + (G_o - G_\infty)e^{-\beta t} \quad (3)$$

where t denotes time, G_o denotes the short-term shear modulus, G_∞ denotes the long-term modulus, and β denotes the viscous decay constant. As reported by Zhang et al. [20], the form for the shear modulus function and its parameters were determined based on in vitro data obtained from vibration tests of the human brain [21]. The values of density and bulk moduli for these brain tissues in the current study were also taken from those specified by Zhang et al. [20] as being the most accurate. All material model parameters for the white and gray matter are listed in Tables 1 and 2.

The CSF, which resides in the ventricles and subarachnoid spaces within the head, is known to be a Newtonian fluid with density and viscosity similar to those of water [22]. For the current study, we have assumed the CSF to be identical to water and have employed a nonlinear tabular equation-of-state for water to represent its mechanical response. However, at the stress levels encountered in our simulations, the CSF effectively acts like an incompressible fluid with a bulk modulus of 1.96 GPa. The properties for the CSF appear in Table 1.

Dry air, the last material employed in our simulations, envelops the head at ambient conditions, occupies the sinuses, and transmits the blast wave. Our model describes the properties of a mixture of N_2 (78.09%), O_2 (21.95%), and Ar (0.96%), defined by a nonlinear tabular equation-of-state model that has been specifically designed for shock wave applications [23]. The tabular format of the EOS for dry air does not lend itself to brief description by equation. However, its compressibility properties are readily viewed graphically and been plotted in Fig. 2. The reference values employed for density and bulk modulus of dry air at ambient conditions are listed in Table 1.

We have selected the material models described above based on their accuracy and relevance to the problem at hand. Whenever possible, we have chosen models that have been validated against head impact data provided by Nahum et al. [24]. To date, however, the events we have simulated in the present study, i.e., the

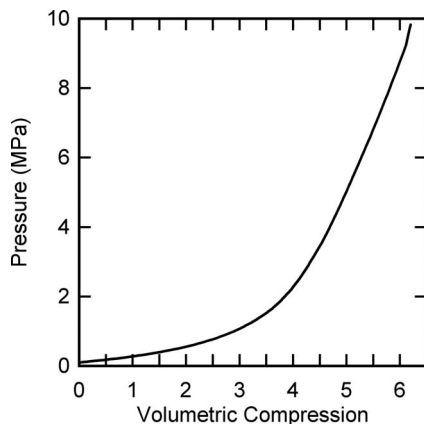


Fig. 2 Compression curve describing the volumetric response for dry air, generated from the tabular equation-of-state model representing the air surrounding the head and occupying sinuses

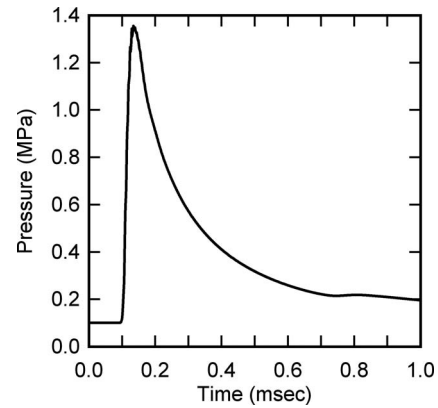


Fig. 3 Wave form of approximated air blast structure of 1.3 MPa (13 bars) magnitude

exposure of a human head to an air blast wave, have not been conducted in a laboratory setting using either an instrumented cadaver or physical model. As such, we are unable to perform a comprehensive validation of our head model and its constituent model representations. In view of this limitation, our approach in the current study has been to qualitatively analyze our simulation results to identify new mechanisms that could lead to brain damage and, therefore, necessitate further examination.

2.4 Blast Simulations. Simulations of direct blast exposure of the head were conducted from three principal directions, anterior (front), posterior (rear), and lateral (right side). The simulation results were analyzed to identify and map sites within the brain experiencing high levels of stress. We also investigated the influence of doubling the blast strength from two of the three directions: anterior and lateral.

We selected blast conditions within the marginal limits of pressure and pulse width for threshold lung damage, defined by the corrected Bowen survivability curve for primary blast injury [25]. We chose these conditions to investigate blast injury scenarios that were otherwise predicted to be survivable. These blast conditions were equivalent to those predicted for a location 2–3 m distant from a detonated explosive device constructed from a 3 kg charge of Octol explosive.

Our blast scenarios were simulated by first positioning the head model in an atmosphere of air at ambient conditions. A slab of energized air, held at conditions of elevated energy and pressure, was positioned 16 cm from the head at time zero. At times greater than zero, mass flow was permitted to occur from the slab of energized air thereby generating a blast wave. The amplitude and pulse width of the blast wave were determined by setting the energized air to predefined conditions of energy, pressure, and slab thickness. This procedure was employed to generate a blast wave of 1.3 MPa (13 bars) magnitude propagating through ambient air in the direction of the head model. The structure of this blast wave is illustrated in Fig. 3.

The blast wave was permitted to envelop the head before being absorbed by transmitting boundary conditions positioned downstream from the head. The boundary condition at the base of the neck was also transmissive, where, across this boundary at $Z=0$, the neck is effectively extended (below $Z=0$). This condition allowed stress waves to propagate across the lower Z -boundary without reflection and, as such, will not influence the early-time wave mechanics of the calculations occurring prior to any significant rigid body motion of the head.

A typical blast simulation required 31 h using 64 processors on the Sandia National Laboratories Thunderbird computer to integrate out to a time of 2 ms for a 16.72×10^6 cell calculation.

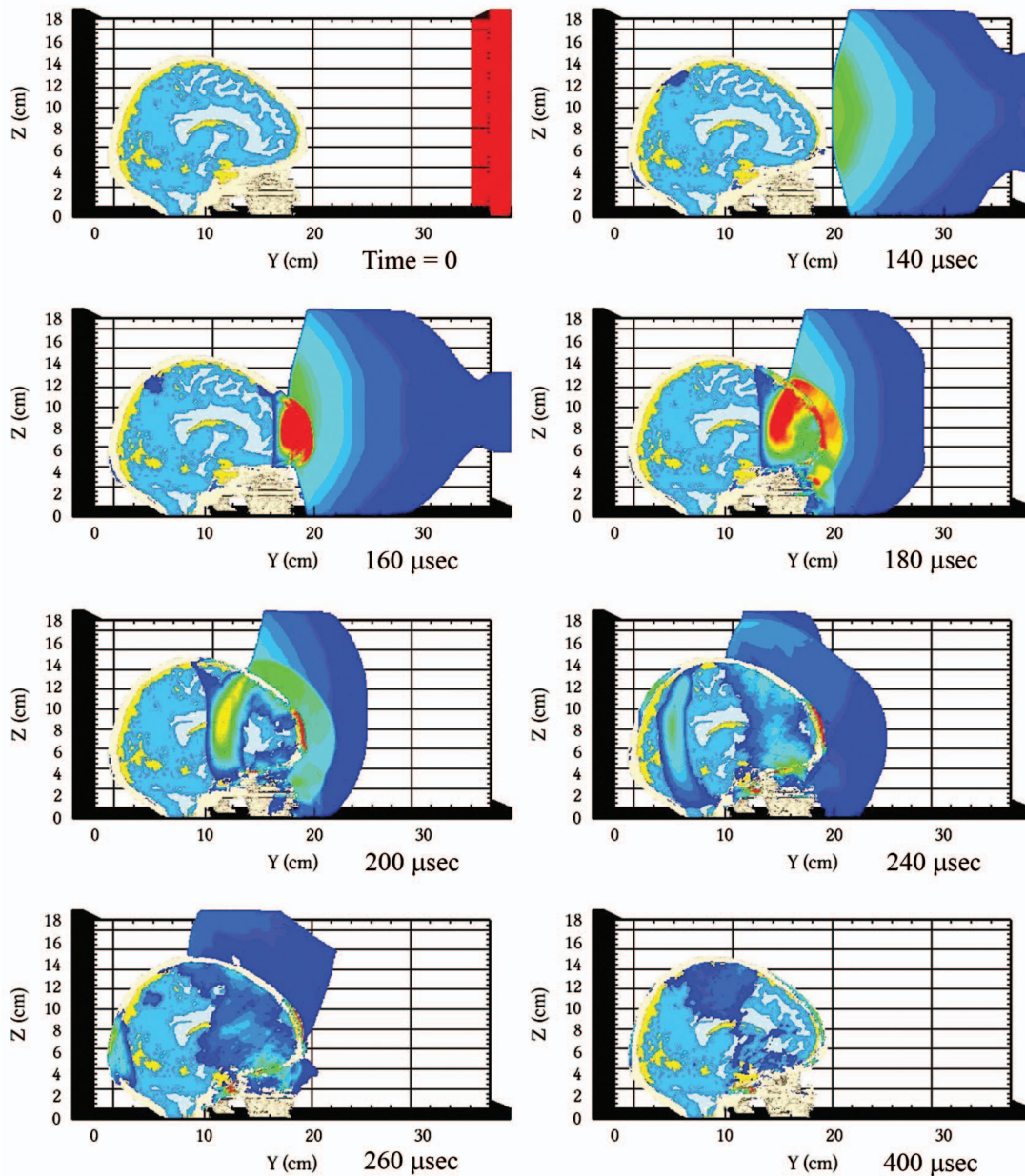


Fig. 4 Midsagittal view of 1.3 MPa frontal blast scenario at various times. Plots are external and intracranial pressure distributions. Color scale: blue=0.11 MPa and red=5 MPa.

3 Results

Three orientations of blast exposure were simulated out to 2 ms each. This time interval was selected by observing that the majority of the intracranial wave mechanics had played out by that time, and the associated stress peaks had been established. Figure 4 illustrates the time-lapse process in a frontal blast simulation in the midsagittal plane, where the blast wave propagates in the air from right to left, envelops the head, and continues downstream in the minus Y -direction. The plots displayed in Fig. 4 show pressure magnitudes between the limits of 0.11 MPa (blue) and 5 MPa (red). Although the pressure history is played out rather early in the simulations, i.e., by $\sim 500 \mu\text{s}$, the deviatoric (shear) stresses within the brain tissue continue to evolve over the full 2 ms time-scale due to the viscoelastic nature of the tissue.

Although the time-lapse evolution of stress wave propagation is intriguing to observe, it is not useful to study the intracranial stress distribution at each time step in an attempt to draw a cor-

relation with brain injury. For this reason, we elected to monitor the maximum values of pressure, volumetric tension, and shear at each point in the head, as these stresses developed over the complete extent of the 2 ms simulation period. We also placed Lagrangian tracer points to record stress level histories at locations in the brain, where axonal injury has been observed in TBI victims. For example, tracer points were positioned, in the corpus callosum, internal capsule, anterior temporal, and at gray matter-white matter junctions.

Figure 5 shows plots of maximum pressure and volumetric tension reached in a midventricular axial plane over the 2 ms simulation time. Note that the regions of highest pressure directly correlated with closest proximity to the blast source. Regions of maximum volumetric tension occurred primarily at sites opposite to the blast source, sometimes referred to as the contrecoup site. Figure 6 shows similar plots of maximum pressure and tension in a midsagittal plane. Maximum pressures between 3 MPa and 4

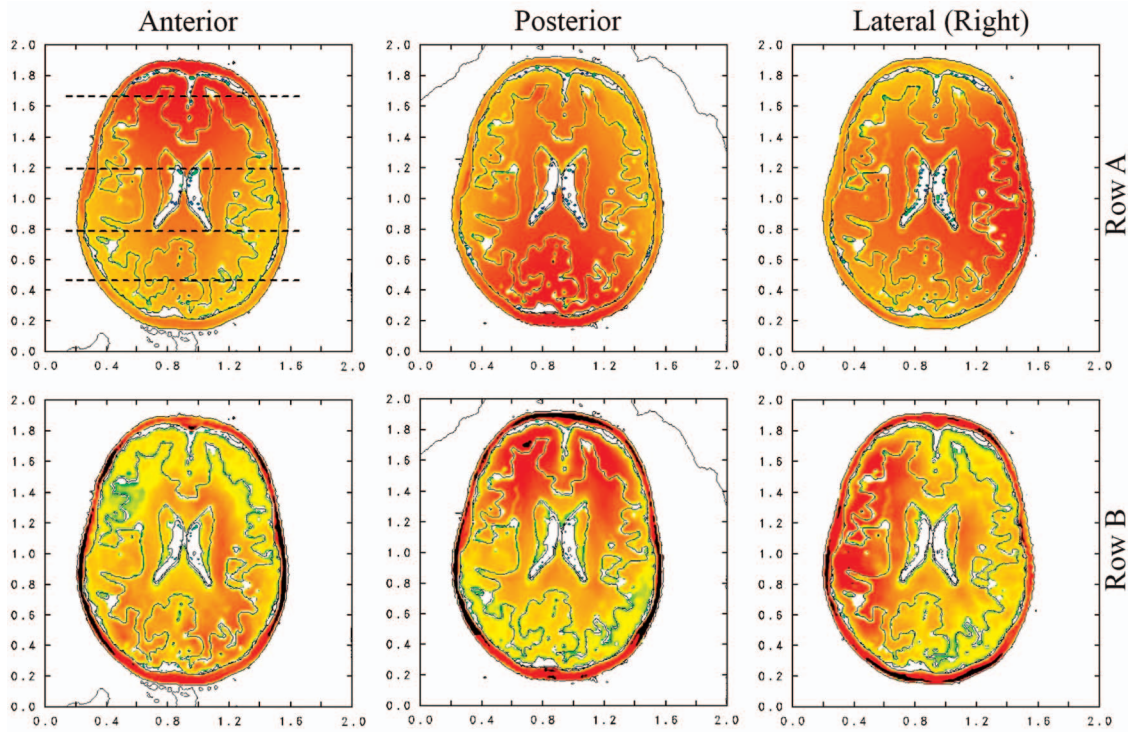


Fig. 5 Maximum pressure (row A) and volumetric tension (row B) in a midventricular axial plane for anterior, posterior, and right lateral blast orientations, where red indicates the highest values and blue the lowest. Note that tension values are negative relative to pressure. Scale: Row A: blue=1 KPa, red=6 MPa; and Row B: blue=1 KPa, red=1.2 MPa. The horizontal dashed lines in the upper left figure indicate the location of the coronal planes shown in Fig. 7.

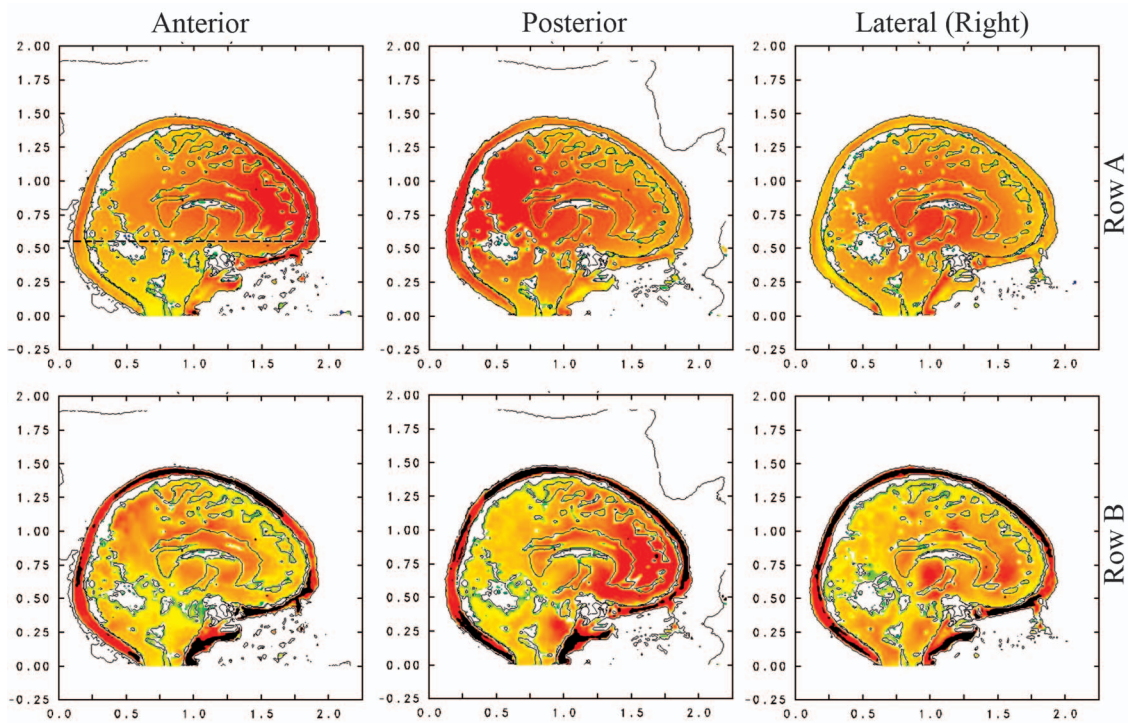


Fig. 6 Maximum pressure (row A) and volumetric tension (row B) in a midsagittal plane for anterior, posterior, and right lateral blast orientations, where red indicates the highest values and blue the lowest. Note that tension values are negative relative to pressure. Scale: Row A: blue=1 KPa, red=6 MPa; and Row B: blue=1 KPa, red=0.9 MPa. The dashed line in the upper left figure indicates the location of the axial images shown in Fig. 8, row A.

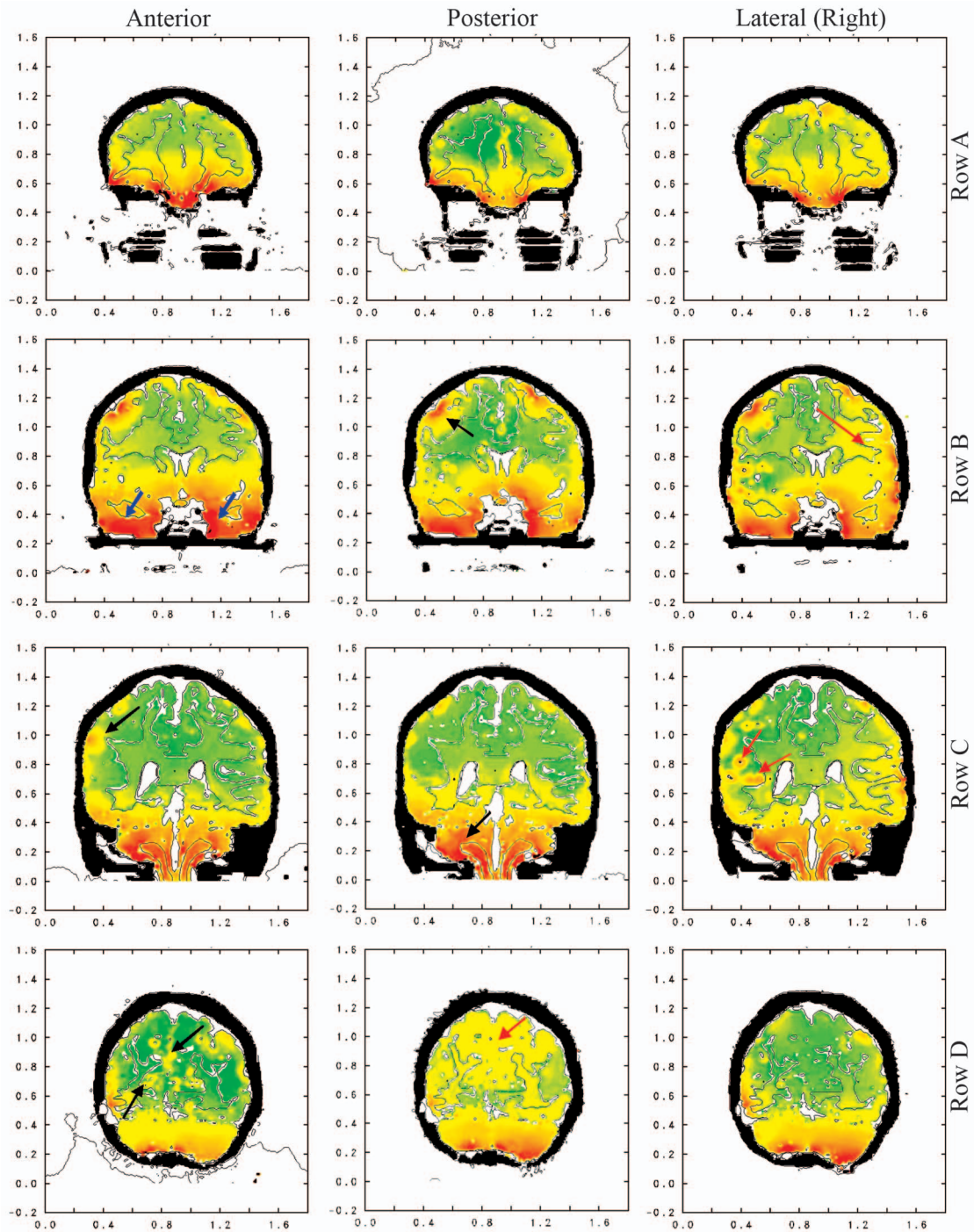


Fig. 7 Maximum deviatoric stress in representative coronal planes for anterior, posterior, and right lateral blast orientations. Scale: (all rows): blue=0.1 KPa, red=15 KPa. Rows A–D correspond to the horizontal dashed lines appearing in the upper left image of Fig. 5. Arrows indicate regions of focal or diffusely elevated shear stress discussed in the text.

MPa (30–40 bars) consistently occurred on the blast side of the head, while maximum tensions of up to 0.8 MPa (8 bars) were observed on the contralateral side.

Comparisons of deviatoric stress in coronal sections between the three blast orientations are presented in Fig. 7. The approximate locations of the coronal sections are shown by the horizontal dashed lines in the upper left image of Fig. 5. The most anterior slice at 15.5 cm (row A) shows only modest differences in shear distributions between anterior, posterior, and lateral blasts. The

coronal slice at 12 cm (row B) displays elevated shear stress in the temporal lobes (blue arrows) and in the cortical area (black arrow) for both anterior and posterior blast orientations. In the lateral blast scenario, elevated shear was diffusely distributed in the right hemisphere (red arrow) in comparison to the contralateral hemisphere which experienced a focal stress pattern. The coronal slice at 8 cm (row C) includes parietal and temporal lobes and passes through the posterior horns of the lateral ventricles. In this plane there were similar shear stress distributions from anterior and pos-

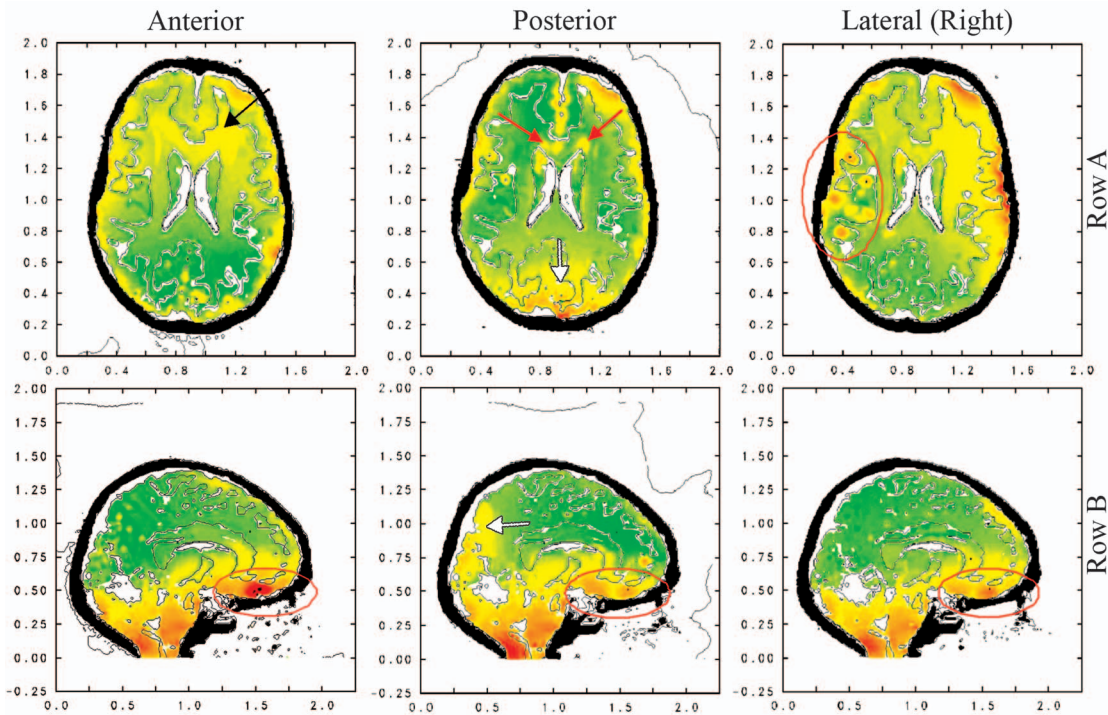


Fig. 8 Maximum deviatoric (shear) stress in a midventricular axial plane (row A) and midsagittal plane (row B) for anterior, posterior, and right lateral blast orientations. Scale: Row A: blue=0.1 KPa, red=15 KPa; and Row B: blue=0.1 KPa, red=25 KPa. Arrows and ovals indicate regions of focal or diffusely elevated shear stress discussed in the text.

terior blast orientations. The highest levels of shear stress occurred in the inferior regions and cortical areas (black arrows). In contrast, prominent focal areas of high shear stress developed in gray matter and at the gray-white matter junctions in the lateral blast scenario (red arrows). Row D images at 4.5 cm represent the coronal plane located in the posterior brain region including the cerebellum and occipital lobes. Focal areas of elevated shear stress in this slice occurred more prominently with anterior blast (black arrows), while overall shear levels were higher and diffusely distributed throughout the slice in the posterior blast scenario (red arrow).

The three-dimensional complexity of shear stress distribution can be appreciated by comparing Figs. 8 and 7. Figure 8 shows areas of maximum shear stress in the same midventricular axial plane as that displayed in Fig. 5 and the same midsagittal plane displayed in Fig. 6. The axial images in Fig. 8 (row A) show considerable differences in shear localization in all three blast scenarios. More focal areas of elevated shear were seen in the lateral blast scenario (multiple red areas within the red oval), whereas the anterior corpus callosum showed greater diffuse shear in the anterior blast (black arrow) but focal shear localizations in the posterior blast (red arrows). The occipital area (white arrow) was most affected in the posterior blast scenario. In the midsagittal views (row B), all blast orientations generated higher shear in the subfrontal regions (red ovals) and brainstem areas. Posterior blast was the only scenario generating high shear stress levels near the midline occipital region (white arrow).

Time-resolved histories of pressure, volumetric tension, and deviatoric stress were recorded for each Lagrangian tracer specified within the head model. Unfortunately, the tracer locations had to be defined prior to execution of the simulations. As a result, many tracers were placed in regions different from those experiencing maximal stress levels during the calculations. However, several of the tracer point histories were highly revealing. Four tracer histories (points 64–67) were positioned in a brain slice located below the lateral ventricles and passing through temporal and frontal

lobe regions (Fig. 9). The axial position of this slice is denoted by the horizontal dashed line displayed in the upper left image of Fig. 6. Pressure and shear stress data from these tracer points are shown in Figs. 10 and 11. For all tracer points in these figures, the shear stress continued to evolve over the full 2 ms simulation period compared with the much more transient pressure wave excursions, which were essentially over within the first 0.8 ms (800 μ s).

Differences in peak pressure timing reflect the varying distances from blast origin to each tracer point. Oscillations or ringing of the pressure wave is prominent, with tracer points 64 and 65 also experiencing significant volumetric tension (negative pres-

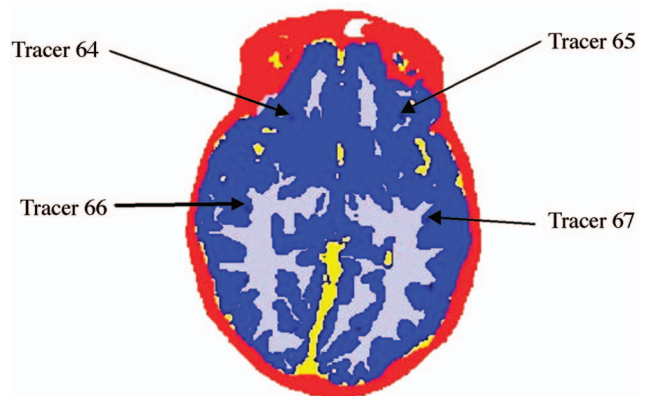


Fig. 9 Tracer point examples in an axial slice below the lateral ventricles, passing through frontal and temporal lobes. The axial position of this slice is identified by the horizontal dashed line in the upper left image of Fig. 6. Red=skull bone, dark blue=gray matter, light blue=white matter, and yellow=cerebral spinal fluid.

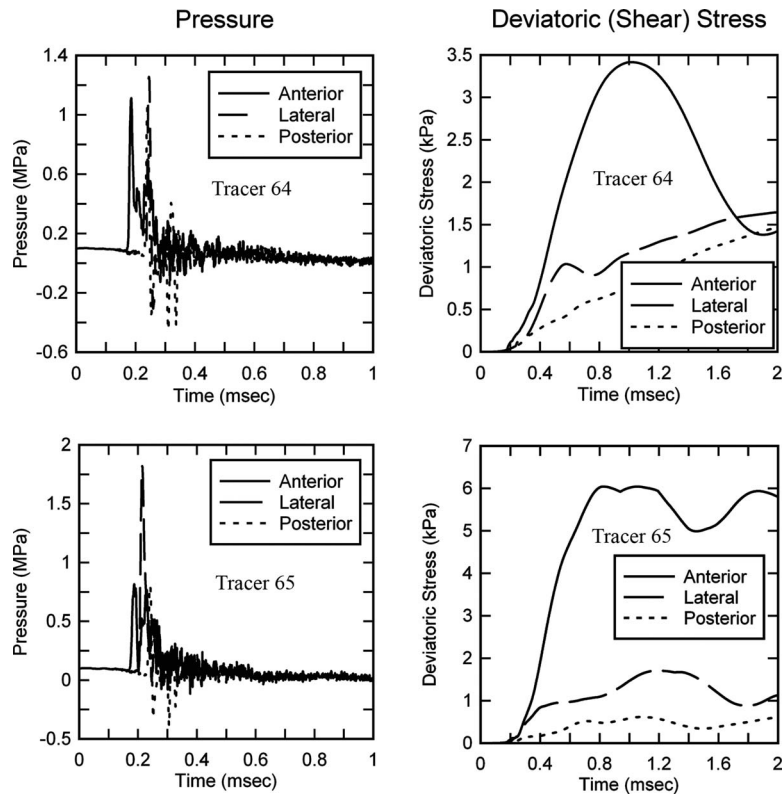


Fig. 10 Pressure (left) and deviatoric stress (right) at tracer locations 64 and 65 located in the frontal lobes of the axial slice in Fig. 9. The deviatoric stress plots are equivalent to von Mises stress.

tures) up to 0.4 MPa (Fig. 10). As noted previously, regions of maximum pressure developed on the side closest to the blast and were highest in the lateral blast scenario. The nominal peak pressure of the blast wave prior to interaction with the skull was 1.3 MPa. However, as a result of differences in acoustic impedance between the air and skull, the pressure wave shocked up to a value of over 4 MPa at the air-skull interface. As the 4 MPa stress wave propagated across the thickness of the skull toward the skull-brain interface, the reduction in acoustic impedance from the skull to the brain caused a reduction in magnitude of the stress wave as it propagated into the brain. As a consequence, the maximum pressure at tracer point 67 was 2.7 MPa in the lateral blast scenario (Fig. 11).

The even numbered tracers (64 and 66) were positioned in the left hemisphere and odd numbered tracers (65 and 67) in the right (Fig. 9). Frontal lobe tracers 64 and 65 experienced the highest shear stress levels from anterior blast (solid curves, Fig. 10), while temporal lobe tracers 66 and 67 experienced maximal shear from lateral blast (dashed curves, Fig. 11). The anterior blast scenario caused a distinctive left-right asymmetry in the shear stress maximum at frontal lobe tracers 64 (3.4 KPa) and 65 (~6 KPa), as depicted in Fig. 10. In contrast, the lateral blast simulation predicted left-right asymmetry (Fig. 11) in the shear maximum between the temporal lobe tracers 66 (1.5 KPa) and 67 (0.58 KPa).

We also conducted simulations of anterior and posterior blast loading to the head with a blast wave possessing double the strength of the 1.3 MPa wave depicted in Fig. 3. For these cases, the blast wave displayed a pulse width similar to that of the 1.3 MPa wave, but with amplitude of 2.6 MPa. The resulting stress distributions predicted in these simulations were qualitatively similar to those from the 1.3 MPa blast predictions, displaying similar regions of elevated stress distributions but with the stress levels approximately doubled.

These results predict wave motion and stresses on time scales significantly shorter than those calculated in other investigations of impulse loading to the head [20,26–29]. The explanation for this important observation has two parts. First, the degree of resolution of our computational mesh is significantly greater than the finite element approximations employed in previous models, and second, the solution algorithms employed in our simulation code are explicit in nature, relying on the Courant condition [30] to determine the appropriate time step. Specifically, we have used a head model (illustrated in Fig. 1) that is resolved into 1 mm cubic voxels with the surrounding air also represented at the same 1 mm resolution. The solution scheme implemented in CTH employs an integration time step that is constrained by the Courant condition to be less than the transit time of the fastest wave disturbance across the smallest cell dimension in the calculation. For the simulation results presented here, the time step was calculated to be a little less than 200 ns ($\sim 2.0 \times 10^{-7}$ s). At this time step, wave disturbances on the order of 2 MHz can be resolved. Consequently, the solution scheme employed here possesses the ability to resolve wave disturbances that occur on significantly shorter timescales than those resolved by solution methods based on implicit solution techniques or employing larger cell or element sizes [31]. This aspect of our simulation approach permits us to highly resolve both the wave mechanics occurring between the blast wave and the head model and the intracranial wave motions that ensue.

4 Discussion

We have conducted a modeling and simulation investigation of the wave motion that occurs within the human brain as a result of blast loading to the head. The results predict significant levels of pressure and deviatoric (shearing) stress occurring at focal regions

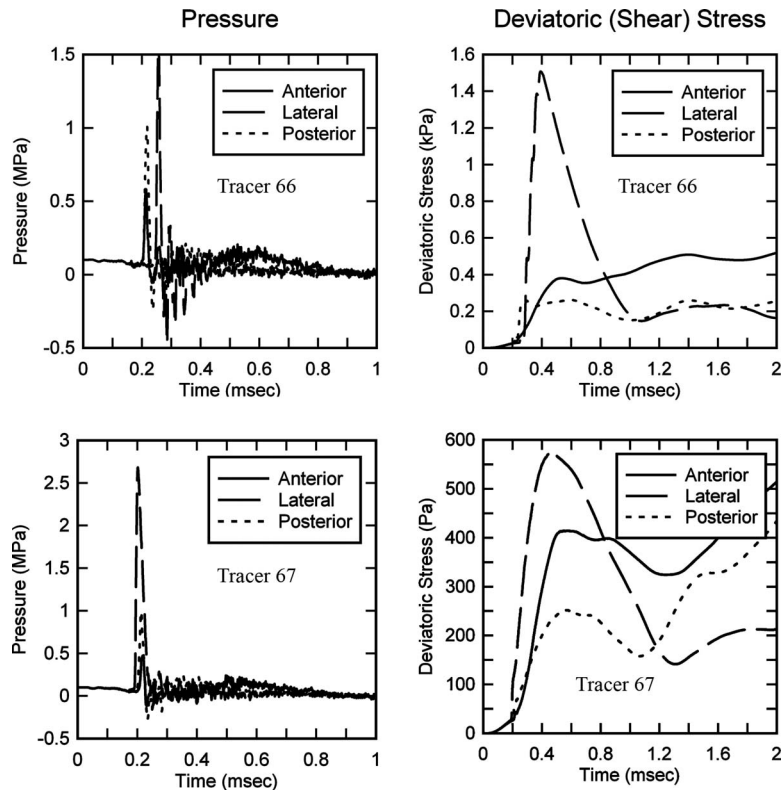


Fig. 11 Pressure (left) and deviatoric stress (right) at tracer locations 66 and 67 located in the temporal lobes of the axial slice in Fig. 9. The deviatoric stress plots are equivalent to von Mises stress.

in the brain within the first 2 ms of the blast event. To our knowledge, this is the first report of a simulation-based investigation of blast-induced intracranial wave phenomenon occurring within the first few milliseconds of blast exposure.

A study conducted by Zhang et al. [32] of football collisions predicted shear stress levels of 3.1–6.4 KPa (mean of 4.5 KPa) in the thalamus that were associated with concussive injury and mild TBI. If these impact calculations represent an injury threshold for shear stress, then we propose that the similar stress levels we calculated in the brain from wave motion alone will be significant. Furthermore, our simulations imply that blast-induced shear stresses can develop on a time scale shorter than that associated with the intracranial accelerations typically linked to TBI, where significant translational and rotational accelerations tend to develop over a time span of 5–20 ms [33].

It is interesting to note that the blast-induced intracranial shear stresses we predict are of comparable magnitude to those generated as a result of impact with a shear-supporting projectile [20]. Our simulations suggest that the head need not be subjected to external shear loads caused by a shear-supporting impactor to experience shear stresses. The fact that the skull and brain tissue are shear-supporting materials is sufficient for shear waves to form as a result of interaction with a strictly dilatational blast wave. Furthermore, the shear wave amplitudes are magnified at material boundaries, and interfaces that exist between the skull, gray matter, and white matter.

Although we found no reports in the literature correlating pressure levels with axonal injury, our blast simulations predict significant blast pressure magnification (\sim threefold) once the pressure waves have transited through the skull and into the brain. The simulations also show that these waves introduce pressure peaks and subsequent volumetric tension to brain tissue over very short periods of time (\sim 0.1–0.2 ms). These brief, relatively high magnitude compression-tension excursions may represent an addi-

tional mechanism for axonal damage, specifically the potential for cavitation or microvoid nucleation within the brain. Although there are a number of analytical and laboratory studies to support the cavitation hypothesis ([34,35]), no clinical evidence yet exist to corroborate its connection to brain injury as a result of impact or blast.

A considerable body of work exists on experimental models and computer simulations of impact loading to the head [20,27–29,36–42]. These studies have established the role of brain accelerations in the development of diffuse axonal injury and its consequences. Based on the present study, we believe that early-time wave action will also occur after blunt impact and may contribute to the overall injury associated with TBI by that mechanism. This possibility is supported by our preliminary study of impact to the head [43]. One of the interesting questions related to mild and moderate TBI is why the outcomes can be so different between patients with similar severity of injury, loss of consciousness, or initial Glasgow Coma Scale score. Even TBI patients with normal conventional brain MRI scans can suffer enduring disability in memory, information processing, and other cognitive domains [44]. Why does one TBI patient return to normal life activities without obvious sequelae while a similarly injured subject does not? One explanation could be that eloquent areas of the brain or critical connections are either damaged or spared at the microscopic level. The evolution of impact or blast-induced wave action, influenced by complex individual head geometry and tissue interfaces, might explain some of the variability in outcome. This mechanism is especially plausible in injuries involving little or no head motion, for example assaults with blunt objects and perhaps primary blast injury.

Our calculations represent an initial step in exploring the role of wave action at early times in the development of axonal injury after blast or impact loading. The head model used in this study is highly resolved and incorporates constitutive models with associ-

ated properties for five constituent materials. The high resolution of the model allows our calculations to capture the early-time evolution of wave action that would not be possible with the larger size of volume elements typically used in finite element calculations. However, our head model currently lacks several structures likely to be important to improving the fidelity of the simulations and validating the predictions with actual brain injury metrics. For example, our model currently does not include the tentorial membranes and falx. Both of these tough fibrous structures would represent an interface and physical boundary separating left and right hemispheres and cerebral from infratentorial structures. Furthermore, we have modeled the biological materials as homogeneous and isotropic. However, this is not the case for the bony material of the skull and the white matter tracks (e.g., corpus callosum) of the brain. In future studies we plan to improve our head model to include the intracranial membranes, as well as to account for porosity of the skull and anisotropy of the white matter tissue. As we have mentioned earlier, our material models have yet to be fully validated against experimental data on blast exposure of an instrumented cadaver or physical model. In future work, we will overcome this shortcoming through collaboration with experimental blast research efforts developing calibrated physical models.

5 Conclusion

In summary, we have conducted simulations of blast injury to the human head and calculated the evolution of intracranial wave action over the first 2 ms after blast exposure. Our results suggest that significant levels of pressure, volumetric tension, and shear stress can occur in focal areas of the brain, dependent on the orientation of the blast wave and the complex geometry of the skull, brain, and tissue interfaces. The focal development of stress or strain energy could exceed the threshold for axonal injury and contribute to the development of TBI and its neurological consequences. If the significance of this early-time mechanism is confirmed, the current understanding of the mechanisms for TBI will need to be modified to include this phenomenon, in addition to the later time brain accelerations and rotations commonly thought to underlie axonal injury.

A better understanding of the physical mechanisms underlying TBI is critical to the development of mitigation strategies involving the design of helmets and other protective gear. The present work suggests that the role of intracranial wave action will need to be considered in designing head protection equipment against blast. A reliable, validated simulation method for blast and impact injury would clearly facilitate the development of protection strategies over a wide variety of injury scenarios where it would be impossible to replicate each event experimentally.

Acknowledgment

Sandia is a multiprogram laboratory operated by Sandia Corporation, a Lockheed Martin Co., for the United States Department of Energy's National Nuclear Security Administration under Contract No. DE-AC04-94AL85000. The authors would like to express their gratitude to Michael Dwyer, Director of Technical Imaging Development, Buffalo Neuroimaging Analysis Center (BNAC), Jacobs Neurological Institute, University at Buffalo, for segmenting the color cryosections for the head model used in this study. We would also like to thank Dr. M.E. Kipp for his insightful technical review of the manuscript.

References

- [1] Centers for Disease Control and Prevention, 2007, "Traumatic Brain Injury in the US: Emergency Department Visits, Hospitalizations, and Deaths," CDC, http://www.cdc.gov/ncipc/pub-res/TBI_in_US_04/TBI_ED.htm.
- [2] Fischer, H., 2007, "United States Military Casualty Statistics: Operation Iraqi Freedom and Operation Enduring Freedom," Library of Congress, Washington, DC, Technical Report No. RS22452.
- [3] Warden, D., 2006, "Military TBI During the Iraq and Afghanistan Wars," *J. Head Trauma Rehabil.*, **21**(5), pp. 398–402.

- [4] DePalma, R. G., Burris, D. G., Champion, H. R., and Hodgson, M. J., 2005, "Blast Injuries," *N. Engl. J. Med.*, **352**(13), pp. 1335–1342.
- [5] Taber, K. H., Warden, D. L., and Hurley, R. A., 2006, "Blast-Related Traumatic Brain Injury: What Is Known?" *J. Neuropsychiatry Clin. Neurosci.*, **18**(2), pp. 141–145.
- [6] Buki, A., and Povlishock, J. T., 2006, "All Roads Lead to Disconnection? – Traumatic Axonal Injury Revisited," *Acta Neurochir. Suppl. (Wien)*, **148**(2), pp. 181–193.
- [7] Smith, D. H., Meaney, D. F., and Shull, W. H., 2003, "Diffuse Axonal Injury in Head Trauma," *J. Head Trauma Rehabil.*, **18**(4), pp. 307–316.
- [8] Adams, J. H., Graham, D. I., Murray, L. S., and Scott, G., 1982, "Diffuse Axonal Injury Due to Nonmissile Head Injury in Humans: An Analysis of 45 Cases," *Ann. Neurol.*, **12**(6), pp. 557–563.
- [9] Graham, D., Gennarelli, T., and McIntosh, T., 2002, *Greenfield's Neuropathology*, Vol. 2, Trauma, Arnold, Hodder Headline Group, London.
- [10] Smith, D. H., Chen, X. H., Xu, B. N., McIntosh, T. K., Gennarelli, T. A., and Meaney, D. F., 1997, "Characterization of Diffuse Axonal Pathology and Selective Hippocampal Damage Following Inertial Brain Trauma in the Pig," *J. Neuropathol. Exp. Neurol.*, **56**(7), pp. 822–834.
- [11] Strich, S., 1961, "Shearing of Nerve Fibers as a Cause of Brain Damage Due to Head Injury: A Pathological Study of Twenty Cases," *Lancet*, **2**(1), pp. 443–448.
- [12] Povlishock, J. T., and Katz, D. I., 2005, "Update of Neuropathology and Neurological Recovery After Traumatic Brain Injury," *J. Head Trauma Rehabil.*, **20**(1), pp. 76–94.
- [13] Povlishock, J. T., Becker, D. P., Cheng, C. L., and Vaughan, G. W., 1983, "Axonal Change in Minor Head Injury," *J. Neuropathol. Exp. Neurol.*, **42**(3), pp. 225–242.
- [14] Reeves, T. M., Phillips, L. L., and Povlishock, J. T., 2005, "Myelinated and Unmyelinated Axons of the Corpus Callosum Differ in Vulnerability and Functional Recovery Following Traumatic Brain Injury," *Exp. Neurol.*, **196**(1), pp. 126–137.
- [15] Nakayama, N., Okumura, A., Shinoda, J., Yasokawa, Y. T., Miwa, K., Yoshimura, S. I., and Iwama, T., 2006, "Evidence for White Matter Disruption in Traumatic Brain Injury Without Macroscopic Lesions," *J. Neurol., Neurosurg. Psychiatry*, **77**(7), pp. 850–855.
- [16] Rugg-Gunn, F. J., Symms, M. R., Barker, G. J., Greenwood, R., and Duncan, J. S., 2001, "Diffusion Imaging Shows Abnormalities After Blunt Head Trauma When Conventional Magnetic Resonance Imaging Is Normal," *J. Neurol., Neurosurg. Psychiatry*, **70**(4), pp. 530–533.
- [17] Hertel, E., Bell, R., Elrick, M., Farnsworth, A., Kerley, G., McGlaun, J., Petney, S., Silling, S., and Taylor, P., 1993, "CTH: A Software Family for Multi-Dimensional Shock Physics Analysis," *Proceedings of the 19th International Symposium on Shock Waves*, Vol. 1, pp. 377–382.
- [18] National Institutes of Health, 2007, "The Visible Human Project," National Library of Medicine, http://www.nlm.nih.gov/research/visible/visible_human.html
- [19] Carter, D. R., 1985, "Biomechanics of Bone," *Biomechanics of Trauma*, Appleton-Century-Crofts, Norwalk, CT, pp. 135–165.
- [20] Zhang, L., Yang, K. H., and King, A. I., 2001, "Comparison of Brain Responses Between Frontal and Lateral Impacts by Finite Element Modeling," *J. Neurotrauma*, **18**(1), pp. 21–30.
- [21] Shuck, L. Z., and Advani, S. H., 1972, "Rheological Response of Human Brain Tissue in Shear," *ASME J. Basic Eng.*, **94**, pp. 905–911.
- [22] Ommaya, A. K., 1968, "Mechanical Properties of Tissues of the Nervous System," *J. Biomech.*, **1**, pp. 127–138.
- [23] Hertel, E., and Kerley, G., 1998, "CTH Reference Manual: The Equation of State Package," Sandia National Laboratories, Albuquerque, NM, Report No. SAND98-0947.
- [24] Nahum, A. M., Smith, R., and Ward, C. C., 1977, "Intracranial Pressure Dynamics During Head Impact," *Proceedings of the 21st Stapp Car Crash Conference*, Society of Automotive Engineers, Inc., Warrendale, PA, pp. 339–366.
- [25] Gruss, E., 2006, "A Correction for Primary Blast Injury Criteria," *J. Trauma: Inj., Infect., Crit. Care*, **60**(6), pp. 1284–1289.
- [26] Horgan, T., and Gilchrist, M., 2004, "Influence of FE Model Variability in Predicting Brain Motion and Intracranial Pressure Changes in Head Impact Simulations," *Int. J. Crashworthiness*, **9**(4), pp. 401–418.
- [27] Nishimoto, T., and Murakami, S., 2000, "Direct Impact Simulations of Diffuse Axonal Injury by Axial Head Model," *JSAE Rev.*, **21**(1), pp. 117–123.
- [28] Suh, C., Kim, S., and Hwang, B., 2005, "Finite Element Analysis of Brain Damage Due to Impact Force With a Three Dimensional Head Model," *Advances in Fracture Strength*, **297–300**(1), pp. 1333–1338.
- [29] Willinger, R., Kang, H. S., and Diaw, B., 1999, "Three-Dimensional Human Head Finite-Element Model Validation Against Two Experimental Impacts," *Ann. Biomed. Eng.*, **27**(3), pp. 403–410.
- [30] Courant, R., Friedrichs, K., and Lewy, H., 1928, "On the Partial Difference Equations of Mathematical Physics," *Mathematische Annalen*, **100**, pp. 32–74.
- [31] Lapidus, L., and Pinder, G., 1982, *Numerical Solutions of Partial Differential Equations in Science and Engineering*, Wiley, New York, NY.
- [32] Zhang, L., Yang, K. H., and King, A. I., 2004, "A Proposed Injury Threshold for Mild Traumatic Brain Injury," *ASME J. Biomech. Eng.*, **126**(2), pp. 226–236.
- [33] Viano, D. C., Casson, I. R., Pellman, E. J., Bir, C. A., Zhang, L., Sherman, D. C., and Boitano, M. A., 2005, "Concussion in Professional Football: Comparison With Boxing Head Impacts—Part 10," *Neurosurgery*, **57**(6), pp. 1154–1172.

- [34] Brennen, C. E., 2003, "Cavitation in Biological and Bioengineering Contexts," Fifth International Symposium on Cavitation, CAV2003, Osaka, Japan, pp. 1–9.
- [35] Lubock, P., and Goldsmith, W., 1980, "Experimental Cavitation Studies in a Model Head-Neck System," *J. Biomech.*, **13**, pp. 1041–1052.
- [36] King, A. I., 1993, "Progress of Research on Impact Biomechanics," *ASME J. Biomech. Eng.*, **115**, (4B), pp. 582–587.
- [37] King, A. I., Ruan, J. S., Zhou, C., Hardy, W. N., and Khalil, T. B., 1995, "Recent Advances in Biomechanics of Brain Injury Research: A Review," *J. Neurotrauma*, **12**(4), pp. 651–658.
- [38] Ruan, J. S., Khalil, T., and King, A. I., 1991, "Human Head Dynamic Response to Side Impact by Finite Element Modeling," *ASME J. Biomech. Eng.*, **113**(3), pp. 276–283.
- [39] Ruan, J. S., Khalil, T., and King, A. I., 1994, "Dynamic Response of the Human Head to Impact by Three-Dimensional Finite Element Analysis," *ASME J. Biomech. Eng.*, **116**(1), pp. 44–50.
- [40] Zhou, C., Khalil, T., and King, A. I., 1994, "Shear Stress Distribution in the Porcine Brain Due to Rotational Impact," *Proceedings of the 38th Stapp Car Crash Conference*, Vol. 38, Society of Automotive Engineers, Inc., Warrendale, PA, pp. 133–143.
- [41] Zhou, C., Khalil, T., and King, A. I., 1995, "A New Model Comparing Impact Response of the Homogeneous and Inhomogeneous Human Brain," *Proceedings of the 39th Stapp Car Crash Conference*, Vol. 39, Society of Automotive Engineers, Inc., Warrendale, PA, pp. 121–137.
- [42] Zong, Z., Lee, H. P., and Lu, C., 2006, "A Three-Dimensional Human Head Finite Element Model and Power Flow in a Human Head Subject to Impact Loading," *J. Biomech.*, **39**(2), pp. 284–292.
- [43] Taylor, P., and Ford, C., 2007, "Simulation of Early-Time Head Impact Leading to Traumatic Brain Injury," *International NeuroTrauma Letter of the International Brain Injury Association*, http://www.internationalbrain.org/enews/issue1_07/index.html.
- [44] Kraus, M. F., Susmaras, T., Caughlin, B. P., Walker, C. J., Sweeney, J. A., and Little, D. M., 2007, "White Matter Integrity and Cognition in Chronic Traumatic Brain Injury: A Diffusion Tensor Imaging Study," *Brain*, **130**(10), pp. 2508–2519.